



Grain-boundary refinement in wire-arc directed energy deposition of duplex stainless steel via in-process ultrasonic vibration

Antoine Queguineur^{1,3} · Olli Wiikinkoski¹ · Mohammad Hallaji¹ · Gaurav Mohanty² · Jean-Yves Hascoët³ · Iñigo Flores Ituarte¹

Received: 2 September 2024 / Accepted: 8 July 2025
© The Author(s) 2025

Abstract

Wire-arc directed energy deposition (WA-DED) is the subject of extensive research in metal additive manufacturing (AM). This study investigates the influence of ultrasonic vibration (UV) on the material properties of deposited ER2209 duplex stainless steel filler wire and evaluates the effects of UV treatment on walls fabricated both with and without weaving. The results demonstrate the effectiveness of a specially developed UV table prototype, showing clear impacts on grain size and ferrite content in the deposited samples. UV treatment reduces the primary ferrite grain width and enhances phase distribution homogeneity, potentially influencing the ferrite-to-austenite transformation during successive reheating cycles. Although the effects on surface morphology and hardness were minimal, significant microstructural changes occurred within the deposited material. UV-induced grain refinement modifies the austenite content, revealing a beneficial interaction between vibration and phase evolution. The UV table design provides a valuable foundation for reproducibility; nevertheless, further optimization of the setup is required to improve performance and support its integration into advanced industrial applications.

Keywords Additive manufacturing · Directed energy deposition · Stainless steel · Ultrasonic vibration · WA-DED · Grain refinement

Recommended for publication by Commission I - Additive Manufacturing, Surfacing, and Thermal Cutting

✉ Antoine Queguineur
antoine.queguineur@tuni.fi

Olli Wiikinkoski
olli.wiikinkoski@tuni.fi

Mohammad Hallaji
mohammad.hallaji@tuni.fi

Gaurav Mohanty
gaurav.mohanty@tuni.fi

Jean-Yves Hascoët
jean-yves.hascoet@ec-nantes.fr

Iñigo Flores Ituarte
inigo.floresituarte@tuni.fi

¹ Faculty of Engineering and Natural Sciences-Automation Technology and Mechanical Engineering, Tampere University, 33720 Tampere, Finland

² Faculty of Engineering and Natural Sciences-Materials Science and Environmental Engineering, Tampere University, 33720 Tampere, Finland

³ Ecole Centrale de Nantes, GeM-UMR CNRS 6183, 1 Rue de La Noé, 44321 Nantes, France

1 Introduction

Directed energy deposition (DED), a category of additive manufacturing (AM) as per ASTM 52900 [1], utilizes an energy source to melt materials, either in powder or wire form. DED techniques are increasingly used in industrial applications such as naval and energy sectors, where process selection influences deposition rate, capacity, and material quality with benefits in terms of environmental impact [2–6]. Wire-arc directed energy deposition (WA-DED) is a subset of DED that uses an electric arc to melt a metallic filler metal and is based on gas metal arc welding (GMAW). WA-DED achieves a high deposition rate, from 3 to 10 kg/h, while maintaining good material characteristics [7, 8].

Higher deposition rate increases the arc energy (AE), which affects grain size and material properties. Balancing the deposition rate and the mechanical–microstructural properties is crucial. Widely used in industrial applications due to their corrosion resistance and mechanical properties, duplex stainless steels (DSSs) exhibit complex microstructural evolution under additive manufacturing conditions. Most steel grades are sensitive to epitaxial growth in WA-DED

with rapid fusion and repeated thermal cycles promoting large grain-oriented structures leading to anisotropic material properties [6, 9]. Using a DSS ER2209 filler metal as defined by the AWS-5.9 standard [10], Zhang et al. [11] have reported a columnar ferrite grains structure with epitaxial growth across the layers leading to anisotropic mechanical properties. The dual phase nature of DSS is of particular interest due to its solidification occurring ferritically, followed by austenite precipitation within the 1300–800 °C temperature range. Zhang et al. [12] have summarized the austenite transformation process as primarily occurring at the grain boundaries, with grain boundary austenite (GBA), followed by the formation of Widmanstätten austenite (WA) and intragranular austenite (IGA) within the ferrite matrix. The numerous reheating cycles during deposition can lead to substantial secondary austenite precipitation as reported by Posch et al. [6]. The objective of 40/60 ferrite to austenite ratio is a typical AM requirement for DSS applications [13, 14]. Excessive ferrite content has been shown to negatively affect impact toughness at low temperatures [15]. Studies on WA-DED using ER2209 filler metal revealed a range of ferrite content from 30 to 65% depending on a variation of deposition parameters [2, 6, 8, 16]. Applying similar AE, ER2209 filler metal exhibits a lower ferrite content than ER2205 [8]. It is attributed to its higher nickel content as nickel is known to promote the austenite formation [17].

In AM applications, various techniques for grain size control are employed either in-process or post-process and include methods such as shot peening, rolling, and thermal control. Ultrasonic shot peening induces plastic deformation in the as-deposited layer, promoting recrystallization at the interlayer bands and resulting in finer grains [18]. Interlayer cold or hot rolling generates many dislocations refining the microstructure, while reducing porosity in the material via plastic deformation [19, 20]. Precise control of the heating and cooling cycles influences grain size and phase distribution [21]. Adding an external system that mechanically affects the as-deposited layers can significantly complicate the manufacturing process, particularly for parts with complicated path planning. Furthermore, extensive post-fabrication heat treatments may introduce considerable part distortion, limiting their applicability for large components. Other techniques that influence grain refinement while maintaining a high deposition rate must address these considerations to facilitate the industrialization of the WA-DED process.

A novel technique emerges with the use of ultrasonic vibration (UV) to affect the microstructure. A few studies have investigated how vibration frequency affects grain size in single or multilayer deposits [22]. Ji et al. [23] demonstrated through computational fluid dynamics (CFD) simulation that UV induces pressure variations in the molten pool, causing cavitation and shock waves, impacting temperature fields and layer morphology in single beads. More research

has focused on austenitic stainless 316L, reporting significant grain refinement, defect reduction, and partial transition from columnar to equiaxed grains [24]. Vorontsov et al. [25] observed a reduction of δ -ferrite volume fraction when using UV, which was associated with a partial transition to an equiaxed microstructure, improving the mechanical properties. Despite previous studies already focusing on various materials, a substantial gap remains in understanding the effect of UV-assisted grain refinement on ER2209 filler metal. Additionally, details regarding the manufacturing of UV systems and their operating parameters are often insufficient for ensuring reproducibility and to enhance the adoption of this technology in AM.

This work aims to evaluate the impact of UV on the microstructure of walls deposited from ER2209 filler wire and to assess its potential for microstructural refinement. The influence of UV in ER2209 could affect the austenite precipitation through finer ferrite microstructure. Using UV to control the microstructure could reduce the reliance on conventional parameters such as voltage (V), current (I), and wire feed speed (WFS), enabling higher deposition rates while maintaining material properties. This introductory study aims to conduct experiments with consistent parameters, while also sharing an open-access prototype for a UV table to support research toward the production of large-scale AM.

2 Experimental

2.1 Material and manufacturing process

The manufacturing utilized a GMAW machine, TPS CMT-Advanced 4000R (FRONIUS, Wels, Austria) which was integrated with an ABB robot IRB-4600. The chosen synergic program, CMT + P, combines cold metal transfer with a pulsed arc in synergic mode. Four configurations were used, each consisting of a straight monobead wall structure. Each configuration was tested both with and without UV. The experiments included a comparison with and without weaving. To maintain surface uniformity, each layer was applied in alternating directions. The welding torch was kept perpendicular to the substrate, maintaining an average contact tip-to-work distance (CTWD) of 17 mm. The walls were printed with a target height of 40 mm and a length of 120 mm. The number of layers was adjusted as needed to reach this objective. After deposition, samples were extracted from these walls for further analysis. The process parameters, I , V , travel speed (TS), and WFS, are detailed in Table 1. The AE values are derived from the power source signal and calculated using Eq. 1), in accordance with EN 1011–1 [26].

Table 1 Nominal values for process parameters

	UV (yes/no)	Weaving (yes/no)	AE (kJ/mm)	WFS (m/min)	<i>I</i> (A)/ <i>V</i> (V)	TS (mm/s)	Layer height (mm)
ER2209	Yes	No	0.34	5.4	136/19.9	8.0	1.9
	No	No	0.34	5.4	136/19.9	8.0	1.9
	Yes	Yes	0.60	5.4	136/19.9	4.5	1.5
	No	Yes	0.60	5.4	136/19.9	4.5	1.5
Additional parameters							
Interpass temperature (IT)			< 200 °C	Weaving amplitude	12 mm		
CTWD			17 mm	Weaving frequency	2 Hz		
Wall height			≤ 40 mm				
Gas flow			15 L/min				

$$AE = \frac{U \times I}{TS} \tag{1}$$

where *AE* is the arc energy expressed in kJ/mm, *U* the arc voltage in volts (V), *I* the current in amperes (A), and *TS* the travel speed in mm/s.

The selected weaving parameters presented in Table 1 were established with an amplitude of 12 mm and a frequency of 2 Hz. Adopting these settings resulted in a decrease in the *TS* to 4.5 mm/s from the 8 mm/s associated with a straight bead deposition strategy, which increased the *AE* to 0.60 kJ/mm. The *IT* was maintained below 200 °C by measuring the top surface between layers with a contact thermometer.

ER2209 filler metal was used with a 1.2-mm diameter, and the chemical composition is detailed in Table 2. The chosen shielding gas was a mixture of argon (Ar) with 30% helium (He) and 2% carbon dioxide (CO₂). The substrate utilized was S355 low carbon steel, measuring 300 mm by 150 mm and 5-mm thick, without preheating. Before manufacturing, the surface was ground to remove oxidation and then cleaned with ethanol.

2.2 Ultrasonic vibration system

Figure 1a shows the manufacturing robotic cell including the vibration table used in this study, along with the welding torch positioned above the part. The technical drawings, bill of materials, and assembly details of the ultrasonic vibration system are openly accessible on GitHub for the research community [27].

The ultrasonic system employed in the experiments featured a 1200 W I1200-WD-35 K generator (SINAPTEC, Lezennes,

France), Fig. 1b. The converter transforms the electrical output from the generator into mechanical movements at high frequency, thereby producing ultrasonic vibrations, here fixed at 35 kHz. The stepped sonotrode, made of TA6V titanium material, is tuned at half wavelength and consists of two different sections, as shown in Fig. 1c, set to maximize the gain. The amplitude gain is calculated based on the dimensions of the two cross-sections of the sonotrode, as expressed in Eq. 2), resulting in a theoretical gain of 3.41. Given the converter’s displacement amplitude of 12 μm, the consequent theoretical amplitude at the sonotrode extremity, considering the maximal attainable value of the system, was 41 μm.

$$G_A = \sqrt{\frac{A_i}{A_o}} = \frac{u_o}{u_i} \tag{2}$$

where *G_A* is the sonotrode amplitude gain (unitless); *A_o* is the output cross-sectional area of the sonotrode, at the tip; and *A_i* is the input cross-sectional area of the sonotrode, at the converter interface, in mm²; *u_i* is the displacement amplitude at the converter interface, and *u_o* the amplitude at the sonotrode tip in μm.

The vibration waves were perpendicular to the substrate and consequently each printed layer. In this study, the amplitude of the ultrasonic system was initially set to 75% of its maximum capacity, as previously noted. Consequently, the resulting amplitude at the sonotrode was about 31 μm. Figure 1d shows the setup of the pneumatic unit used to maintain a constant contact pressure between the sonotrode and the substrate, essential for transmitting ultrasonic waves to the part during manufacturing. Applying a contact pressure of 5 bars to the pneumatic unit generates a total force of 113.1 N from the 2

Table 2 Filler wire chemical composition (wt-%)

	C	Si	Mn	P	S	Cr	Ni	Mo	Cu	N	Fe
ER2209	0.014	0.48	1.57	0.018	0.001	23.02	8.74	3.14	0.05	0.146	Bal

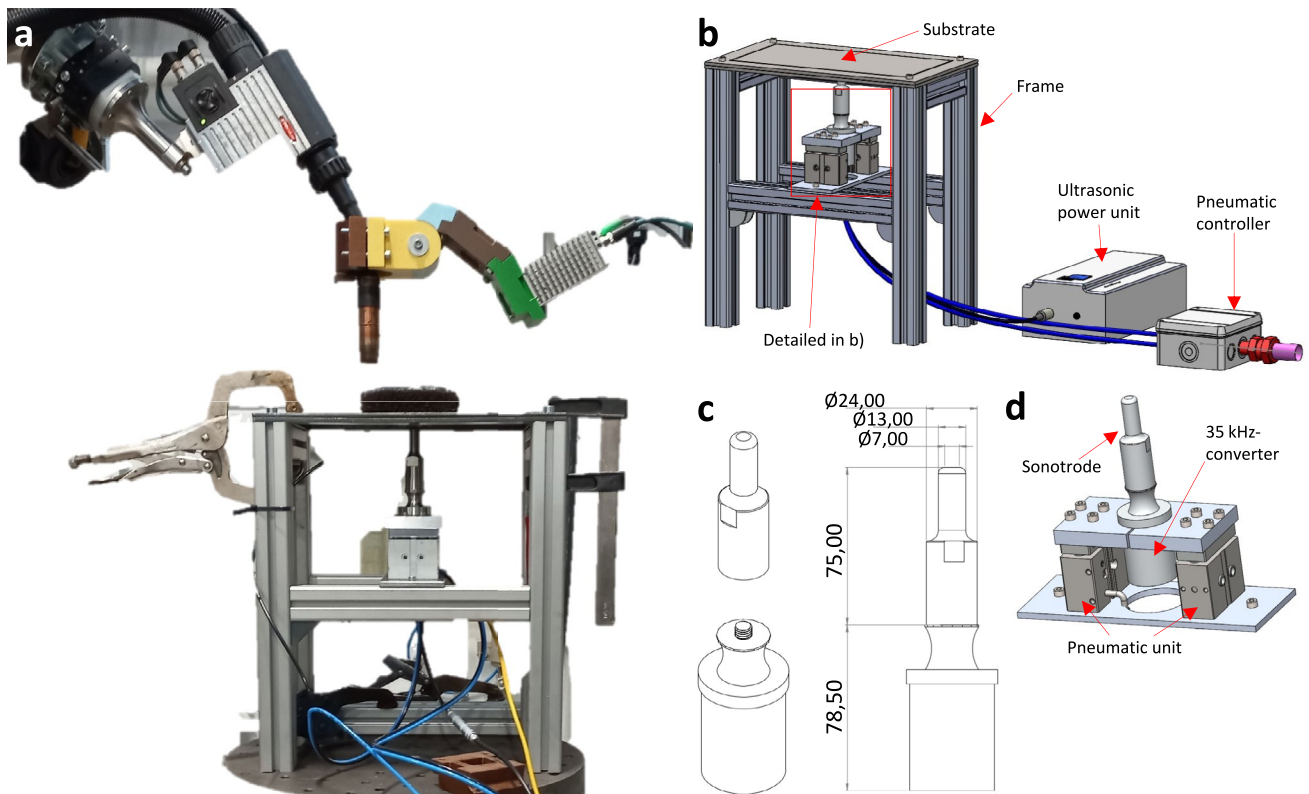


Fig. 1 UV system showing (a) the manufacturing setup, (b) a schematic view of the entire system, (c) the sonotrode, and (d) a detailed view of the subsystem generating vibration

pistons of 12 mm each using Eq. 3). This force is transmitted through the sonotrode to the substrate and ensures effective energy transfer and enhances the efficiency of ultrasonic vibrations.

$$F = P/s \quad (3)$$

where F is the applied force in Newton (N), P the pressure applied in Pascal (Pa), and S the contact area in m^2 .

2.3 Characterization

A FeritScope® testing unit, based on the magnetic induction method, was utilized and installed on a 3-axes Ender-3Pro Cartesian motion platform. The measuring probe, FGAB1.3-Fe (Helmut Fischer GmbH, Sindelfingen, Germany), was automatically positioned, maintaining an approach speed of less than 4 mm/s and a lift-off distance of 20 mm between successive measurement points. FeritScope® measurements were performed across the entire cross-section of each sample, with a fixed spatial resolution of 1 mm. The measurements are depicted in two-dimensional colormaps to visually illustrate the data distribution across the samples and potential variations. The values, presented as a percentage

of ferrite, exclude the areas within 2 mm of the edges, which impact the sensitivity of the FeritScope® measurements.

For the microstructural characterizations, the samples were ground and polished to 1 μm . For the optical characterization of ER2209, a Beraha-II mod. color etchant (170 mL H_2O , 30 mL HCl, and 2 g $K_2S_2O_5$) was used. This etchant selectively colors the ferrite phase, allowing it to be easily distinguished from the austenite phase. All images were taken using a Leica Dmi8 optical microscope. To evaluate the effects of UV on grain structure, cross-sectional sections were analyzed. Ferrite was measured using image analysis with color segmentation using ImageJ software. The method used a similar approach as described in previous research and is based on contrast differentiation in etched cross-sectional samples [8, 28].

A Vickers indenter, mounted on a NEMESIS 5100G2 hardness testing unit (Innovatest, Maastricht, The Netherlands), was used for hardness measurements. Vickers hardness testing (HV10) was performed with a 10 kgf test load and a dwell time of 10 s per indent, in accordance with the recommendations of the EN ISO 6507-1 standard [29]. To obtain comprehensive cross-sectional mapping, spatial resolutions were defined to scan both thin and thick samples in the studied materials. The surface morphology of the deposited walls in all configurations was analyzed using

an Alicona Infinite Focus G5 (Alicona, Graz, Austria) to measure optical surface waviness, achieving a lateral resolution of $4\ \mu\text{m}$. The inspected areas of the samples measured $20\ \text{mm} \times 2.81\ \text{mm}$.

3 Results

Microstructural observations of the walls produced with weaving, with and without UV treatment, are shown in Fig. 2. The two samples responded differently to the etchant; the UV-treated sample appeared slightly more blurred despite identical etching times. Structural variations are visible across both cross-sections after etching. Both samples exhibit columnar grain structures consisting of primary ferrite and austenite, IGA, WA, and localized secondary austenite formed by reheating from subsequent passes. Although the complex phase distribution, especially at low

magnification, makes this difficult to discern clearly, the UV-treated sample shows narrower primary grains. The average ferrite content in the UV-treated, woven sample was $47.8 \pm 3.0\%$, compared to $36.0 \pm 2.4\%$ in the regular configuration. These values reflect averages across all layers, excluding the final deposited layer.

The microstructure of the final deposited layer is noteworthy, exhibiting a higher ferrite content. Although this layer is typically removed by milling in applications, it provides a practical opportunity to examine the effect of UV treatment on the microstructure, as the vibrations primarily influence the molten pool and, consequently, the solidification process. The higher ferrite content is attributed to its as-built condition, without reheating cycles, and to the fact that vibration influences the material during solidification rather than affecting the already solidified metal. The microstructural analysis of the ferrite grain width in the final layer of each wall shows an average spacing of $144 \pm 64\ \mu\text{m}$ with UV treatment, compared

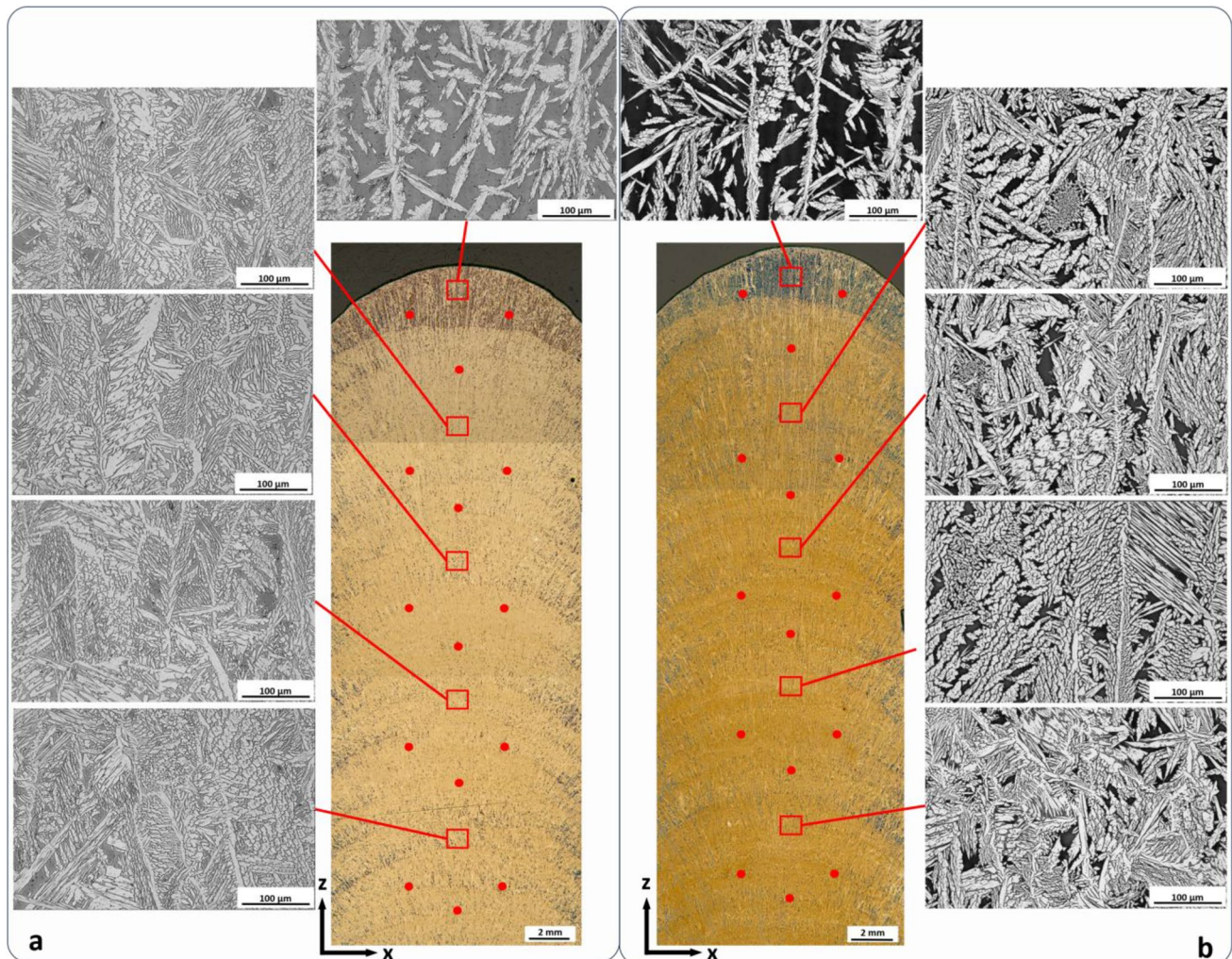


Fig. 2 Cross-sections of multilayer ER2209 walls performed using weaving: (a) with UV and (b) regular deposition (red dots indicate areas where image analysis was used for ferrite measurements)

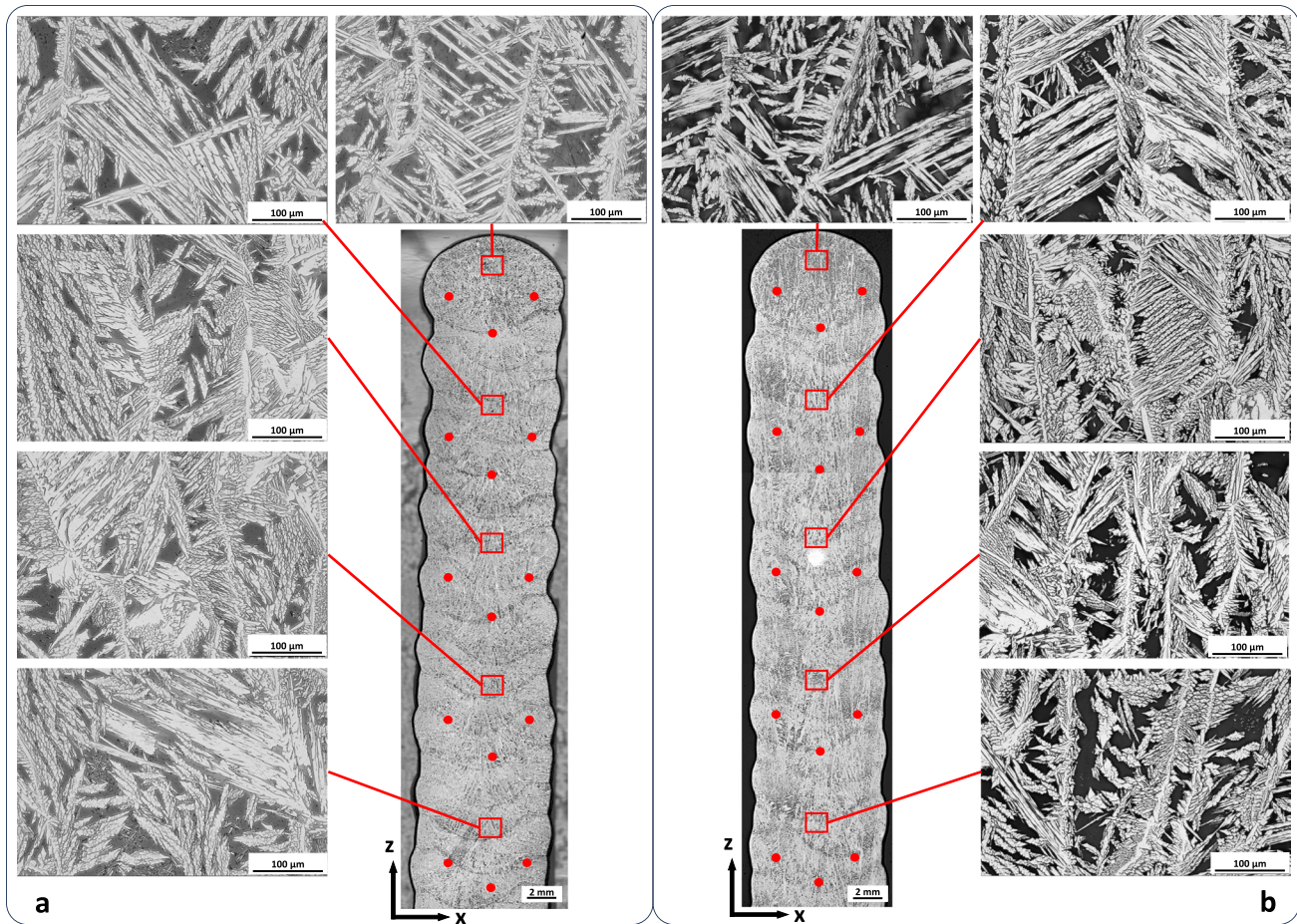


Fig. 3 Cross-sections of multilayer ER2209 walls performed without weaving: **(a)** with UV and **(b)** regular deposition (red dots indicate areas where image analysis was used for ferrite measurements)

to $331 \pm 110 \mu\text{m}$ without UV treatment. Under similar process parameters, the average grain width is significantly reduced under the influence of the UV process.

Cross-sections of walls manufactured without weaving are shown in Fig. 3. The stitched macroscopic image reveals the effect of UV treatment on the grain structure, with a thinner and shorter ferritic columnar structure. In contrast, the wall without UV treatment exhibits large columnar grains. The regularly deposited wall shows a wider grain structure compared to its weaving equivalent. The average ferrite content measured in the samples with UV was $45.0 \pm 2.4\%$ and $42.8 \pm 4.0\%$ in the regular configuration, with the values falling within the standard deviation, showing no significant statistical difference.

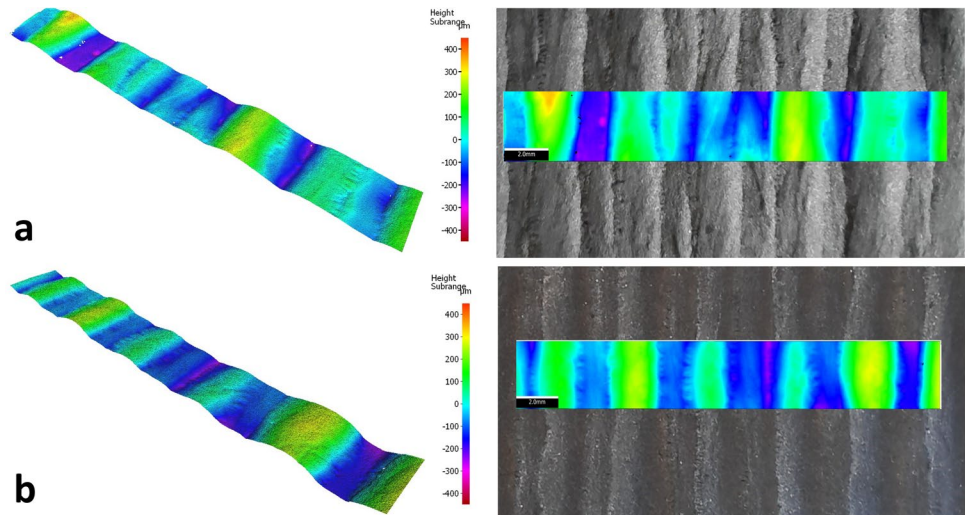
Focusing on the analysis of the last layer in its as-deposited structure, similar measurements of the grain width were conducted. The microstructural analysis shows, in walls without weaving, an average grain width of $113 \pm 34 \mu\text{m}$ with UV treatment and $228 \pm 157 \mu\text{m}$ in the regularly deposited sample.

The wall surface morphologies are presented in Fig. 4 for the samples deposited without weaving. The waviness analysis shows that the surface with UV treatment has a similar overall profile, measuring max. $78 \mu\text{m}$ compared to $83 \mu\text{m}$ without UV. The surface undulations show slight variation, reaching a maximum of $400 \mu\text{m}$ with UV treatment and $380 \mu\text{m}$ without UV.

The evaluation of the ferrite content in the complete cross-section of the walls with a FeritScope® is shown in Fig. 5. No significant variation is observed, with similar ferrite content variations showing a higher percentage in the last layer of each of the four-sample walls studied. The average values for ferrite content were $35.4 \pm 1.3\%$ and $36.3 \pm 1.3\%$, without weaving, and $34.2\% \pm 1.5\%$ and $34.5\% \pm 1.6\%$, for weaving samples, respectively, with and without UV treatment.

The 2-dimensional hardness mapping of the sample cross-section is presented in Fig. 6. Both sets of experiments, with and without weaving, exhibited a wide scatter.

Fig. 4 Surface morphologies of as-deposited ER2209 walls, acquired using an optical profilometer: (a) scanned wall surface with UV and (b) scanned regular wall surface



These results did not indicate significant statistical differences, on average, between the samples. Without weaving, the hardness was $248.3 \pm 4.6 \text{ HV}_{10}$ with UV treatment and $251.1 \pm 5.7 \text{ HV}_{10}$ in regular deposition, while with weaving, it was $244.4 \pm 7.4 \text{ HV}_{10}$ with UV treatment and $247.5 \pm 6.3 \text{ HV}_{10}$ in regular deposition. The hardness was higher in the last deposited layer of the walls, which aligned with the increased ferrite content observed in this region.

4 Discussions

This study investigated how UV treatment applied during deposition affects the microstructure of duplex ER2209 wire deposits fabricated by WA-DED under different processing conditions. While UV treatment did not lead to substantial changes in surface morphology or hardness, it affected the microstructure with a significant refinement of primary ferrite grains and, in some cases, a shift in the ferrite-to-austenite balance. These microstructural changes were especially apparent in the final layers and under weaving conditions, where thermal gradients and reheating cycles differ from standard deposition. No cracks and only minor isolated gas pores ($< 0.2 \text{ mm}$) were observed in all samples, indicating that UV treatment did not influence defect formation under the investigated processing conditions. These findings highlight the potential of UV as a process control tool for tailoring microstructure in multi-pass WA-DED applications.

Additionally, this study contributes to the field through the development of an open-source ultrasonic vibration system. Future investigations may explore the effect of UV on intermetallic phase formation, optimize vibration parameters, and further examine localized transformation behavior during WA-DED.

4.1 Surface quality and hardness

Surface morphology analysis revealed only minor variations in waviness between UV-treated and regular samples, indicating a limited influence of UV on the overall surface topography under the investigated conditions. Ji et al. [23] studied the influence of UV on deposition layer morphology in WA-DED, demonstrating that it promotes a more uniform and refined surface profile. This effect was attributed to enhanced melt pool fluidity and reduced surface waviness resulting from UV-induced cavitation. However, in the present study, this mechanism did not lead to a significant modification of surface waviness at the scale of the wall comprising multiple layers. Further research could explore the impact of different ultrasonic vibration frequencies and amplitudes on surface morphology to better understand their influence.

Hardness measurements did not demonstrate statistically significant differences between samples. Hardness variability can be influenced by several factors, including local ferrite–austenite ratios, grain morphology, and potential presence of intermetallic phases. The slight variations observed likely reflect local microstructural heterogeneities rather than systematic effects of UV treatment.

4.2 Grain refinement and solidification features

Microstructural observations confirmed columnar grain structures composed of ferrite and primary austenite across all samples. The solidification was fully ferritic, with epitaxial growth of the primary ferrite grains, which occurs perpendicular to the solidification front. During cooling, the solid-state transformation from ferrite to austenite begins, influenced by the cooling rate [30]. This transformation initiates at the grain boundaries forming the GBA followed by the precipitation of austenite within

the primary ferrite grains [12]. This eventually forms IGA and WA structures, as observed in Fig. 2. The presence of secondary austenite is attributed to the multiple reheating cycles experienced during the multilayer deposition process. UV-treated samples exhibited noticeably narrower and shorter ferrite grains, particularly in the walls with weaving.

Microstructural variations can be influenced by wall geometry, particularly through differences in wall thickness that affect heat dissipation and, consequently, grain structure. However, the results indicate that the influence of UV treatment remained consistent across the different wall geometries tested. This consistency suggests that the primary effects of UV treatment are likely linked to modifications in melt pool dynamics, rather than being significantly impacted by geometric variations.

In deposited DSS, solidification typically follows the grain orientation of the underlying layer, with competitive grain growth governing the evolution of the dual-phase microstructure [31–33]. Todaro et al. [34] investigated solidification under UV treatment and reported the formation of a wider constitutional supercooling (CS) zone, a region of supercooled liquid ahead of the solidification front. In this zone, the temperature drops below the equilibrium solidification point, promoting nucleation and the growth of new grains. The presence of a wider CS zone in UV-assisted deposition was found to facilitate more uniform grain nucleation and refinement. Although that study focused on ER316L, the fundamental principles are

applicable to DSS, as ER2209, supporting the observation of finer ferrite grains in the present work.

Although grain refinement was confirmed, the UV treatment did not significantly alter the overall grain growth direction or columnar morphology, implying that the fundamental solidification mode remains similar but with finer structural features.

4.3 Ferrite content variation

The most prominent effect of UV treatment was observed in the variation of ferrite content. Analysis of phase balance from both magnetic (Feritscope®) and optical image analysis techniques highlighted method-specific limitations. Magnetic measurements, though useful for general trends over larger surface areas, lack the resolution needed for precise characterization of localized microstructural variations. Optical image analysis remains the high-resolution reference method, despite its limited applicability to extensive surfaces, as previously confirmed by Putz et al. [35]. Quantitative image analysis revealed that, across the full wall thickness, excluding the final layer, UV treatment led to an increase in ferrite content in samples produced with weaving, while only a slight, statistically insignificant increase was observed in the configuration without weaving. However, the final deposited layer, which was not affected by reheating from subsequent passes, exhibited a markedly higher ferrite content compared to the underlying layers. In the configuration without weaving, UV treatment had a limited effect, resulting in a slightly lower ferrite content ($49.5\% \pm 1.9\%$) compared to regular deposition ($51.9\% \pm 1.7\%$), with values falling within the standard deviation. In the samples with weaving, no statistically significant difference was observed, indicating that the influence of UV in the final layer was primarily limited to grain refinement rather than altering the phase balance.

These findings suggest that the effect of UV treatment on phase balance is strongly dependent on the thermal history of the material. In the bulk of the walls, where multiple reheating cycles occur due to subsequent layer deposition, the application of UV may promote localized changes in melt pool dynamics and solute redistribution, leading to a slight increase in ferrite content, especially in configurations with weaving, more thermally affected. UV treatment contributes to grain refinement, but its influence on phase balance is more noticeable in regions subjected to repeated thermal cycles, highlighting the complex interaction between process parameters, heat flow, and phase transformations in DSS.

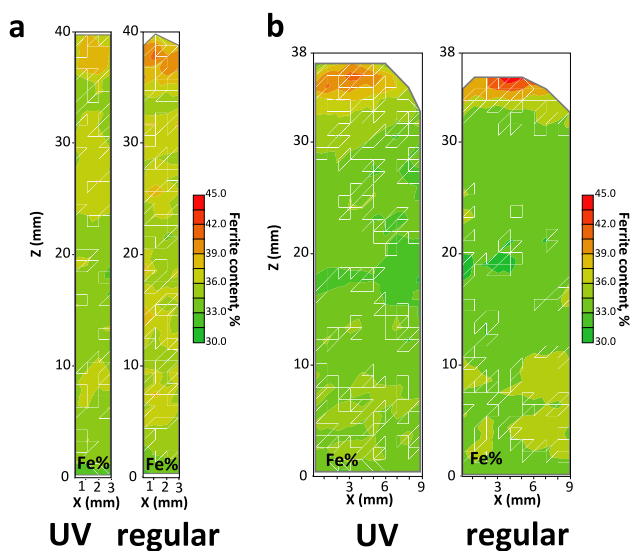


Fig. 5 FeritScope® measurements of a sample (a) without weaving and (b) with weaving

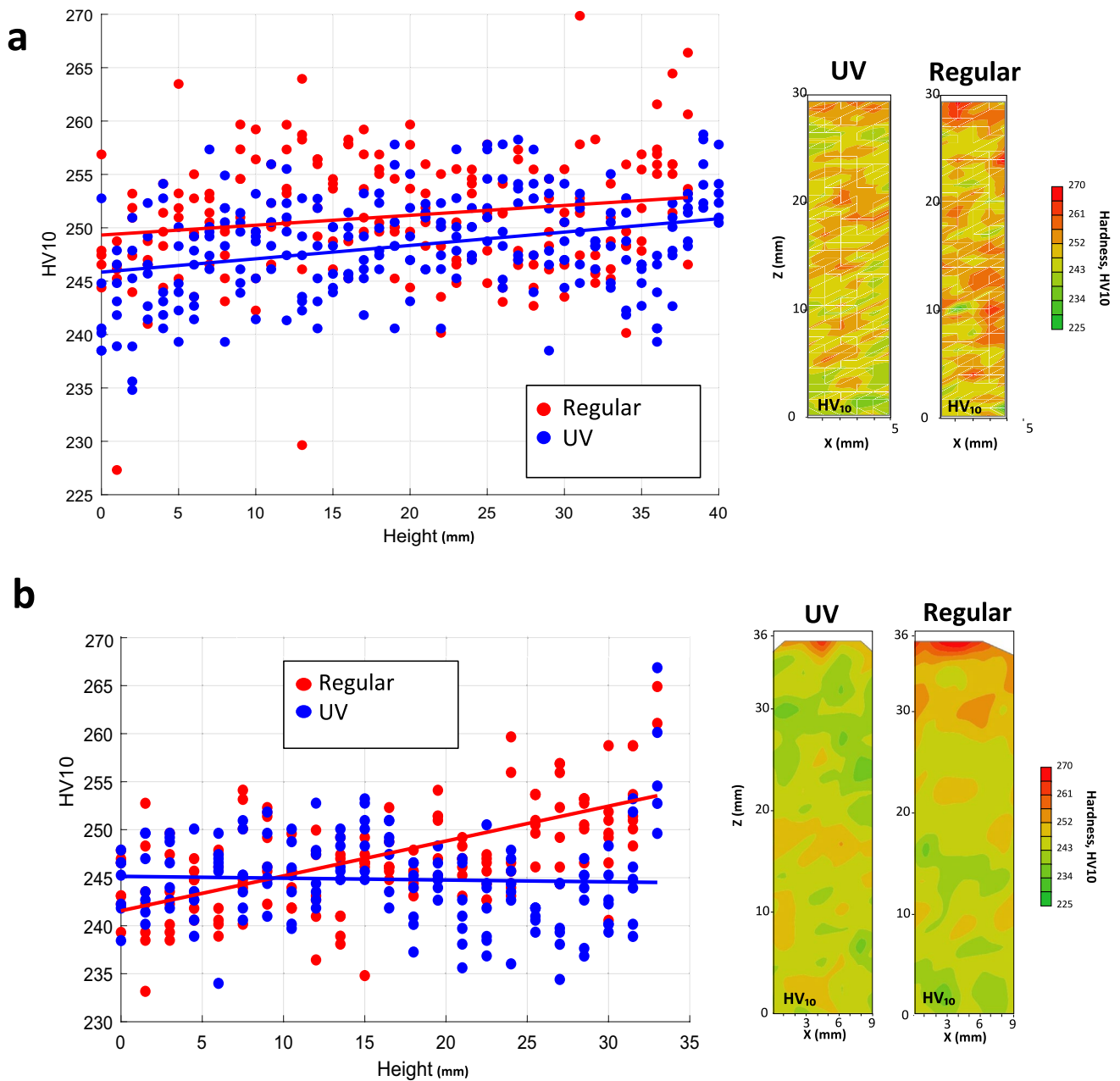


Fig. 6 Hardness (HV_{10}) of UV-treated and regularly deposited ER2209, (a) without weaving and (b) with weaving—and their associated 2-dimensional mapping

5 Conclusions

This study investigates the influence of ultrasonic vibration (UV) treatment during wire-arc directed energy deposition (WA-DED) of duplex stainless steel (DSS) ER2209 wire on microstructure, phase balance, surface features, and hardness. The positive effects of ultrasonic vibration (UV) on the microstructure and phase balance were successfully demonstrated. The main contributions of the study are as follows:

- All samples were free of cracks and showed only minor, isolated porosity, indicating that UV treatment did not adversely affect defect formation.
- UV treatment had minimal impact on surface morphology, with negligible differences in surface waviness across all tested configurations.
- Hardness measurements exhibited significant variability, with no consistent differences observed between UV-treated and untreated samples. This is attributed to

local fluctuations in phase balance and potential microstructural heterogeneities.

- Ferrite grain refinement was clearly observed in UV-treated samples. UV resulted in reduced primary ferrite grain width, including finer and shorter ferrite grains. However, the overall grain growth direction was not significantly affected.
- UV treatment positively influenced the phase distribution with an increase in ferrite content, particularly when applying weaving. This effect is presumably linked to acoustic streaming mechanisms, which enhance elemental mixing, promote homogeneity, and subsequently influence elemental diffusion.

Future research will focus on investigating the potential influence of ultrasonic vibration on the solidification direction, particularly its effect on grain orientation and competitive growth mechanisms in duplex stainless steel.

Author contribution The first draft of the manuscript was written by Antoine Queguineur and Iñigo Flores Ituarte, and all authors commented on previous versions of the manuscript. Antoine Queguineur conceived and designed the experiments. The prototype has been designed and assembled by Olli Wiikinkoski. Material preparation, data collection, and analysis were performed by Antoine Queguineur, Olli Wiikinkoski, and Mohammad Hallaji. All authors read and approved the final manuscript. Iñigo Flores Ituarte, Gaurav Mohanty, and Jean-Yves Hascoët have supervised this study.

Funding Open access funding provided by Tampere University (including Tampere University Hospital). The contributions of Antoine Queguineur, Olli Wiikinkoski, and Mohammad Hallaji acknowledge partial funding support from the Business Finland project TANDEM (4056/31/2021), granted under the SMART EUREKA cluster on Advanced Manufacturing, as well as from the Academy of Finland Research Fellowship (346874)—D2M (Multi-disciplinary Digital Design and Manufacturing).

Data availability The data supporting the findings of this study are available from the corresponding author upon reasonable request.

Declarations

Competing interests The authors declare no competing interests.

Open Access This article is licensed under a Creative Commons Attribution 4.0 International License, which permits use, sharing, adaptation, distribution and reproduction in any medium or format, as long as you give appropriate credit to the original author(s) and the source, provide a link to the Creative Commons licence, and indicate if changes were made. The images or other third party material in this article are included in the article's Creative Commons licence, unless indicated otherwise in a credit line to the material. If material is not included in the article's Creative Commons licence and your intended use is not permitted by statutory regulation or exceeds the permitted use, you will need to obtain permission directly from the copyright holder. To view a copy of this licence, visit <http://creativecommons.org/licenses/by/4.0/>.

References

1. ASTM International (2021) ISO/ASTM 52900:2021 – additive manufacturing – general principles – fundamentals and vocabulary. West Conshohocken, PA: ASTM International. <https://doi.org/10.1520/F3177-21>
2. Pechet G, Hascoet J-Y, Rauch M, Ruckert G, Thorr A-S (2020) Manufacturing of a hollow propeller blade with WAAM process - from the material characterisation to the achievement. *Industry 40 – Shaping the future of the digital world* 155–160. <https://doi.org/10.1201/9780367823085-28>
3. O'Neill F, Mehmanparast A (2024) A review of additive manufacturing capabilities for potential application in offshore renewable energy structures. *Forces Mech* 14:100255. <https://doi.org/10.1016/j.finmec.2024.100255>
4. Monteiro H, Carmona-Aparicio G, Lei I, Despeisse M (2022) Energy and material efficiency strategies enabled by metal additive manufacturing – a review for the aeronautic and aerospace sectors. *Energy Rep* 8:298–305. <https://doi.org/10.1016/j.egy.2022.01.035>
5. Rauch M, Pechet G, Hascoet JY, Ruckert G (2021) Extending high value components performances with additive manufacturing: application to naval applications. *Solid State Phenom* 319:58–62. <https://doi.org/10.4028/www.scientific.net/ssp.319.58>
6. Posch G, Chladil K, Chladil H (2017) Material properties of CMT—metal additive manufactured duplex stainless steel blade-like geometries. *Weld World* 61:873–882. <https://doi.org/10.1007/s40194-017-0474-5>
7. Queguineur A, Marolleau J, Lavergne A, Ruckert G (2020) Evaluation of tandem controlled short-circuit GMAW for improved deposition in additive manufacture of large nickel aluminium bronze naval components. *Weld World* 64:1389–1395. <https://doi.org/10.1007/s40194-020-00925-z>
8. Queguineur A, Asadi R, Ostolaza M, Valente EH, Nadimpalli VK, Mohanty G, Hascoët J-Y, Flores Ituarte I (2023) Wire arc additive manufacturing of thin and thick walls made of duplex stainless steel. *Int J Adv Manuf Technol* 127:381–400. <https://doi.org/10.1007/s00170-023-11560-5>
9. Prathivraj S, Oyyaravelu R (2024) Effect of interpass temperature on austenite ferrite ratio of wire arc additive manufactured 2507 Super Duplex Stainless Steel. *Mater Lett* 361:136125. <https://doi.org/10.1016/j.matlet.2024.136125>
10. AWS A5.9/A5.9M:2022 (2022) Specification for bare stainless steel welding electrodes and rods. American Welding Society, Miami, FL
11. Zhang Y, Cheng F, Wu S (2021) The microstructure and mechanical properties of duplex stainless steel components fabricated via flux-cored wire arc-additive manufacturing. *J Manuf Process* 69:204–214. <https://doi.org/10.1016/j.jmapro.2021.07.045>
12. Zhang D, Liu A, Yin B, Wen P (2022) Additive manufacturing of duplex stainless steels - a critical review. *J Manuf Process* 73:496–517. <https://doi.org/10.1016/j.jmapro.2021.11.036>
13. Iams AD, Keist JS, Palmer TA (2020) Formation of austenite in additively manufactured and post-processed duplex stainless steel alloys. *Metall Mater Trans A* 51:982–999. <https://doi.org/10.1007/s11661-019-05562-w>
14. Zhang Y, Wu S, Cheng F (2022) A specially-designed super duplex stainless steel with balanced ferrite:austenite ratio fabricated via flux-cored wire arc additive manufacturing: microstructure evolution, mechanical properties and corrosion resistance. *Mater Sci Eng. A* 854:13. <https://doi.org/10.1016/j.msea.2022.143809>
15. Kang DH, Lee HW (2012) Effect of different chromium additions on the microstructure and mechanical properties of multipass weld

- joint of duplex stainless steel. *Metall Mater Trans A* 43:4678–4687. <https://doi.org/10.1007/s11661-012-1310-6>
16. Hosseini VA, Högström M, Hurtig K, Valiente Bermejo MA, Stridh LE, Karlsson L (2019) Wire-arc additive manufacturing of a duplex stainless steel: thermal cycle analysis and microstructure characterization. *Weld World* 63:975–987. <https://doi.org/10.1007/s40194-019-00735-y>
 17. Lippold JC, Kotecki DJ (2005) *Welding metallurgy and weldability of stainless steels*. Wiley-VCH, Hoboken
 18. Wang Y, Shi J (2020) Recrystallization behavior and tensile properties of laser metal deposited Inconel 718 upon in-situ ultrasonic impact peening and heat treatment. *Mater Sci Eng, A* 786:139434. <https://doi.org/10.1016/j.msea.2020.139434>
 19. Xu H, Zhang Q, Tian T, Niu L, Li H, Han B, Zhu H, Wang X (2023) In-situ hot rolling directed energy deposition-arc repair of shafts. *Addit Manuf* 61:16. <https://doi.org/10.1016/j.addma.2022.103362>
 20. Gu J, Ding J, Williams SW, Gu H, Ma P, Zhai Y (2016) The effect of inter-layer cold working and post-deposition heat treatment on porosity in additively manufactured aluminum alloys. *J Mater Process Technol* 230:26–34. <https://doi.org/10.1016/j.jmatprotec.2015.11.006>
 21. Mukherjee T, Elmer JW, Wei HL, Lienert TJ, Zhang W, Kou S, DebRoy T (2023) Control of grain structure, phases, and defects in additive manufacturing of high-performance metallic components. *Prog Mater Sci* 138:101153. <https://doi.org/10.1016/j.pmatsci.2023.101153>
 22. Wang H, Hu Y, Ning F, Cong W (2020) Ultrasonic vibration-assisted laser engineered net shaping of Inconel 718 parts: effects of ultrasonic frequency on microstructural and mechanical properties. *J Mater Process Technol* 276:116395. <https://doi.org/10.1016/j.jmatprotec.2019.116395>
 23. Ji F, Qin X, Hu Z, Xiong X, Ni M, Wu M (2022) Influence of ultrasonic vibration on molten pool behavior and deposition layer forming morphology for wire and arc additive manufacturing. *Int Commun Heat Mass Transfer* 130:105789. <https://doi.org/10.1016/j.icheatmasstransfer.2021.105789>
 24. Cong W, Ning F (2017) A fundamental investigation on ultrasonic vibration-assisted laser engineered net shaping of stainless steel. *Int J Mach Tools Manuf* 121:61–69. <https://doi.org/10.1016/j.ijmachtools.2017.04.008>
 25. Vorontsov A, Astafurov S, Melnikov E, Moskvina V, Kolubaev E, Astafurova E (2021) The microstructure, phase composition and tensile properties of austenitic stainless steel in a wire-feed electron beam melting combined with ultrasonic vibration. *Mater Sci Eng, A* 820:141519. <https://doi.org/10.1016/j.msea.2021.141519>
 26. EN 1011–1:2009 (2009) *Welding - recommendations for welding of metallic materials. Part 1. General guidance for arc welding*. European Committee for Standardization (CEN), Brussels
 27. Wiikinkoski O (2024) Ultrasonic vibration table repository. <https://github.com/Digital-Design-and-Manufacturing-D2M/Ultrasonic-vibration-table-for-DED-process>. Accessed 21 Jul 2025
 28. Varbai B, Pickle T, Májlínger K (2018) Development and comparison of quantitative phase analysis for duplex stainless steel weld. *Period Polytech Mech Eng* 62:247–253. <https://doi.org/10.3311/PPme.12234>
 29. EN ISO 6507–1:2018 (2018) *Metallic materials - Vickers hardness test - part 1: test method*. The International Organization for Standardization, Geneva
 30. Zhu C, Zeng J, Wang W, Chang S, Lu C (2020) Mechanism of $\delta \rightarrow \delta + \gamma$ phase transformation and hardening behavior of duplex stainless steel via sub-rapid solidification process. *Mater Charact* 170:110679. <https://doi.org/10.1016/j.matchar.2020.110679>
 31. Westin EM, Valiente Bermejo MA, Axelsson B, Hurtig K, Hagqvist P, Jonsson JY (2025) Enhancing duplex stainless steel additive manufacturing with DED-LB/w: microstructural analysis and process optimization. *Weld World* <https://doi.org/10.1007/s40194-025-02053-y>
 32. Tóth T, Westin EM, Köhler M, Dilger K (2025) Enhancing austenite formation in directed energy deposition-arc fabrication of duplex stainless steel using nitrogen-bearing shielding gas. *Weld World* 69:837–848. <https://doi.org/10.1007/s40194-024-01914-2>
 33. Wittig B, Zinke M, Jüttner S (2021) Influence of arc energy and filler metal composition on the microstructure in wire arc additive manufacturing of duplex stainless steels. *Weld World* 65:47–56. <https://doi.org/10.1007/s40194-020-00995-z>
 34. Todaro CJ, Easton MA, Qiu D, Brandt M, StJohn DH, Qian M (2021) Grain refinement of stainless steel in ultrasound-assisted additive manufacturing. *Addit Manuf* 37:101632. <https://doi.org/10.1016/j.addma.2020.101632>
 35. Putz A, Althuber M, Zelić A, Westin EM, Willidal T, Enzinger N (2019) Methods for the measurement of ferrite content in multipass duplex stainless steel welds. *Weld World* 63:1075–1086. <https://doi.org/10.1007/s40194-019-00721-4>

Publisher's Note Springer Nature remains neutral with regard to jurisdictional claims in published maps and institutional affiliations.